JOURNAL OF SPACECRAFT AND ROCKETS
Vol. 32, No. 6, November–December 1995

Waverider Design for Generalized Shock Geometries

Kevin D. Jones*
U.S. Naval Postgraduate School, Monterey, California 93943-5000
Helmut Sobieczky†
DLR, German Aerospace Research Establishment, D3400 Göttingen, Germany
A. Richard Seebass‡
University of Colorado, Boulder, Colorado 80309-0429
and
F. Carroll Dougherty§
Florida State University, Tallahassee, Florida 32306-4052

A new method for the design of inviscid waverider configurations with more general shock geometries than previously possible is presented. An arbitrary three-dimensional shock shape is specified as input, and a new inverse method, utilizing a cross-stream marching scheme for solving the Euler equations, is used to generate the postshock flowfield. Unlike most previous studies, this approach allows for the use of nonaxisymmetric shock topologies with nonconstant shock strengths. The problem's ill-posedness is suppressed by reformulating the problem in the proper curvilinear coordinate system. The inverse marching approach is briefly summarized, and details of the waverider design procedure are given. Comparisons of individual waveriders and their flowfields generated by the new algorithm in a few seconds on a workstation with flowfields computed by a direct Euler solver, requiring on the order of an hour of Cray 2 CPU time, demonstrate the accuracy and efficiency of the new approach.

Nomenclature

a	= elliptic semiaxis in z direction
a/b	= elliptic axis ratio
b	= elliptic semiaxis in y direction
M_∞	= freestream Mach number
p	= pressure
U, V, W	= contravariant velocity components
u, v, w	= Cartesian velocity components
x, y, z	= Cartesian coordinates
γ	= ratio of specific heats
ζ	= radial computational coordinate
η	= circumferential computational coordinate
ξ	= streamwise computational coordinate
ρ	= density

Introduction

IN the quest for high-speed aircraft, whether for atmospheric flight or for access to space, an old idea, the waverider, has resurfaced as a viable class of such craft. Waveriders, classically defined in inviscid flow, have sharp leading edges and maintain attached shock waves at the design flight conditions. The shock wave is generally contained beneath the body in such a way that the aircraft appears to be riding on the wave; hence the name.

Waveriders are interesting vehicles for several reasons. From a performance standpoint they have, both theoretically and experimentally, provided high values of lift over drag at high Mach numbers at design flight conditions. Recent experimental work[1,2] has shown waveriders to be competitive at off-design conditions as well. From a design standpoint waveriders offer the unique feature of isolating the flows over the upper and lower surfaces, effectively dividing their design into two independent problems. The lower surface is designed to generate a desired shock wave and engine inlet flow conditions, and the upper surface may be independently designed to fulfill performance, internal volume, and other requirements.

Waveriders were first conceptualized as re-entry vehicles for manned space flight.[3] The classic caret wing produced a planar shock wave contained beneath a delta-planform aircraft as illustrated in Fig. 1. The caret-wing was carved from the inviscid, two dimensional, supersonic flow over an infinite wedge. By taking the known flowfield and defining a leading edge on the shock surface (an inverted V shape in this case) the streamsurface passing through the leading edge could be used to define the waverider lower surface. The upper surface was chosen parallel to the freestream flow, defining a body with internal volume. The postshock pressure on the lower surface was higher than the freestream pressure on the upper surface, providing lift.

A similar approach was used to generate waveriders from the flowfields about axisymmetric cones at zero incidence.[4] In the following years many researchers (see Eggers et al.[5] for a summary) provided variations to this design approach using a variety of flowfields from which the waveriders were carved, and including many peripheral computations to predict skin-friction, real-gas, and blunt-leading-edge effects, with some incorporating optimization procedures. However, virtually all past studies (as well as the current

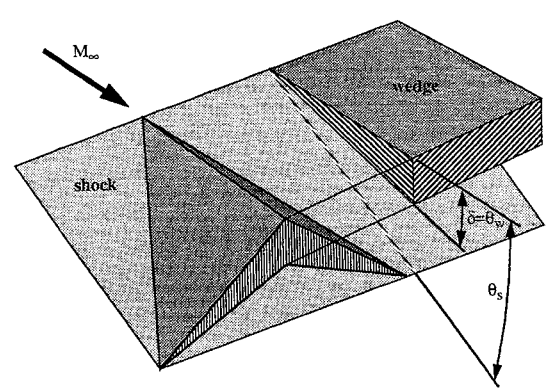

Fig. 1 Nonweiler caret-wing waverider.

Received Sept. 13, 1994; revision received April 24, 1995; accepted for publication April 27, 1995.

*NRC Research Associate, Department of Aeronautics and Astronautics, Mail Code AA/JO. Member AIAA.
†Senior Scientist, DLR SM-TS, 10 Bunsenstrasse. Member AIAA.
‡Professor, Aerospace Engineering Sciences, Campus Box 429. Member AIAA.
§Visiting Scientist, Supercomputing Computations Research Institute. Member AIAA.

study) used inviscid analysis to define the waverider geometry, and only geometrically simple shock shapes such as planes or axisymmetric surfaces were considered, because exact or relatively simple approximate solutions for the postshock flowfields were known.

The design of waveriders is inherently an inverse problem. In Refs. 3 and 4, known flowfields were used to generate waveriders; thus, the configurations were inversely designed to reproduce desired shocks and flowfields. Conceptually it is difficult to design a vehicle that will perform as a waverider at some desired cruise conditions using direct methods. However, it is a relatively simple task to choose a desired shock wave and find the waverider that will generate it. Inverse methods are often superior to direct methods for use in optimization procedures as well. Past work[6,7] has shown that inviscid waveriders can be designed, with a boundary-layer code predicting skin friction, in a few seconds on a workstation using inverse techniques, whereas a direct Navier–Stokes simulation of the same configuration requires the order of an hour of CPU time on a Cray Y-MP. Note that the inviscid–viscous approach taken by these inverse methods assumes that the shock remains attached and that the boundary-layer thickness is very small compared to the waverider thickness (i.e., the waverider geometry is defined by a streamsurface, and no modifications are made to account for boundary layer displacement thickness). The Navier–Stokes simulations predict a slightly detached shock, due to boundary-layer thickness and finite leading-edge roundness, but the pressure data agree well with Euler simulations and experimental data.[8]

The current study again employs an inverse design method with the same basic design approach previously outlined. However, where most past waverider design studies have limited the choice of shock shapes to planar or axisymmetric surfaces, the current work allows for the use of more general shock shapes than those of any previous studies. The method utilizes a noniterative, cross-stream marching scheme that solves the Euler equations to define the flowfield behind a specified shock surface for which the waverider is to be determined. The general, three-dimensional, supersonic cross-stream marching problem is ill posed; however, if the numerical problem is correctly formulated, the method yields accurate and physically meaningful solutions. Skin friction, real-gas effects, and blunt leading edges are not considered in this study. These and other peripheral computations have been successfully used in past studies[6,7] and may be included in future versions of the present design tool.

In this paper, the theory behind the new inverse marching scheme used in the flowfield solution is summarized; details of the peripheral computations used to design the waveriders are given; and comparisons with theory and direct Euler simulations demonstrate the validity of the approach.

Flowfield Solution

The theory leading to the development of the inverse, cross-stream marching algorithm for the Euler equations was given first in Ref. 9 and in greater detail in Ref. 10; the general methodology and a few pertinent details are summarized here. Four basic steps are taken by the marching procedure to define the flowfield behind a given shock surface. First, the shock geometry is defined, and a surface mesh is generated (Fig. 2a); second, the postshock flow conditions are determined using the Rankine–Hugoniot jump relations (Fig. 2b); third, the marching directions are computed, and a new grid layer is generated (Fig. 2c); and, finally, the solution is computed on the new layer. The last two steps are repeated in a step-by-step fashion to define the flow in a bounded domain (Fig. 2d).

Posedness

The virtue of such an inverse scheme is that no knowledge of a generating body is needed to define the flowfield behind a given shock. However, this is also the origin of the problem's ill-posedness. For a mathematical problem to be well posed, a solution must exist and be unique and stable. While the questions of existence and uniqueness are rarely considered for problems such as this, since the governing equations are derived from fundamental laws of mechanics, the question of stability—or, more aptly, the continuous dependence of the solution on initial data—is a valid concern. In other

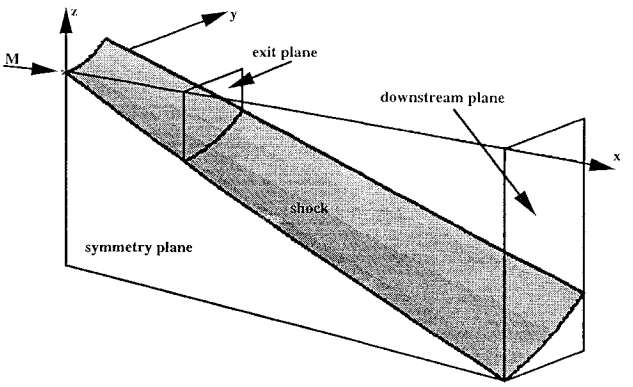

a) Shock surface

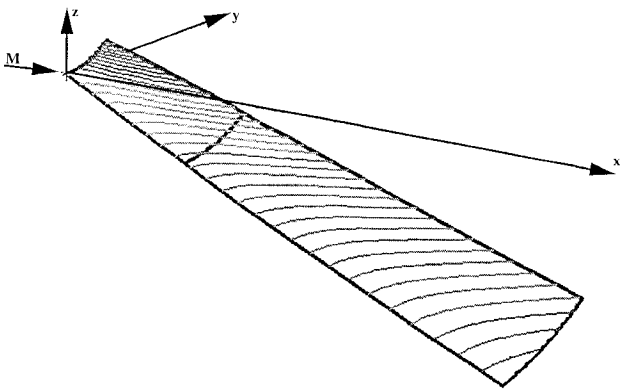

b) Postshock conditions

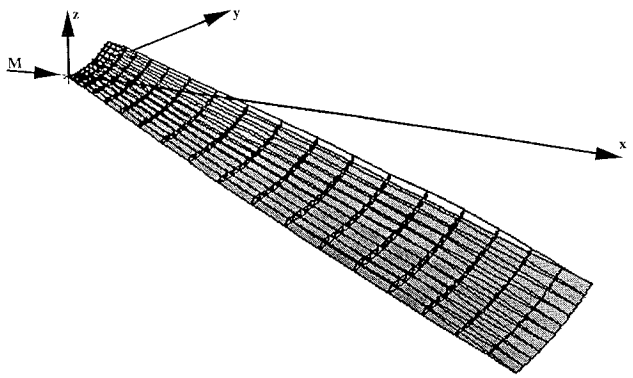

c) Marching grid

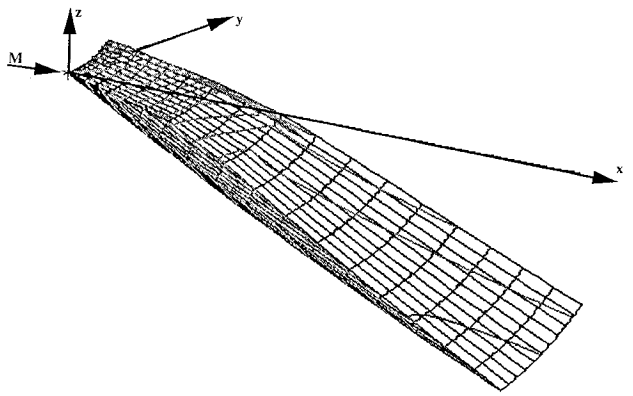

d) Completed flowfield

Fig. 2 Four steps for flowfield definition.

words, do small changes in the initial data result in small changes in the solution, or do they cause large or unbounded changes in the solution?

In three-dimensional flow, the shape of the resulting shock is, in general, quite insensitive to local changes in the body shape, or, inversely, small changes in the shock shape may require large changes in the body shape or, worse yet, may preclude the existence of a solution altogether, thus violating the stability condition for a well-posed problem. It is entirely possible to specify a shock shape for which no solution exists without the inclusion of flow features not allowed here, such as embedded shocks.

A more detailed discussion of the causes and effects of the problem's ill-posedness is documented in Ref. 10, but to illustrate the basic principles a simple, linear model equation is used here:

$$\phi_{xx} - \phi_{yy} - \phi_{zz} = 0 \tag{1}$$

Equation (1) is a linear, hyperbolic equation in three independent variables with x as the timelike (or flow) direction. A solution can be constructed by an infinite series of modal components of the form

$$\phi = \exp[i(k_1 x + k_2 y + k_3 z)] \tag{2}$$

where $i = \sqrt{(-1)}$ and k_1, k_2, and k_3 are the wave numbers in the respective x, y, and z coordinate directions. To march in the usual timelike direction, the wave number k_1 must be determined. Differentiating Eq. (2) and substituting the results into Eq. (1), one obtains the relation

$$k_1 = \pm\sqrt{k_2^2 + k_3^2} \tag{3}$$

such that for all real k_2 and k_3, k_1 is real-valued, and ϕ is bounded for all x.

However, marching in a cross-stream direction implies marching in a direction different from the timelike direction—the z direction in this case. The relation

$$k_3 = \pm\sqrt{k_1^2 - k_2^2} \tag{4}$$

is formed for k_3 as a function of k_1 and k_2. It can be seen that for $|k_2| > |k_1|$, k_3 is imaginary valued, and ϕ is unbounded as $z \to \infty$. Hence, this simple, three-dimensional, cross-stream marching procedure is ill posed, that is, the solution is not continuously dependent on the initial data, unless constraints are placed on the initial data, namely, $|k_2| \leq |k_1|$.

Consider now a similar two dimensional problem with the governing equation

$$\phi_{xx} - \phi_{zz} = 0 \tag{5}$$

with modal components of the form

$$\phi = \exp[i(k_1 x + k_3 z)] \tag{6}$$

To march in the z direction, the wave number k_3 must be determined. It is given by the relation

$$k_3 = \pm\sqrt{k_1^2} \tag{7}$$

Hence, for all real k_1, k_3 is real-valued, and ϕ remains bounded for all z.

In summary, the three-dimensional problem governed by Eq. (1) is well posed only if constraints are placed on the initial data, but the two dimensional problem governed by Eq. (5) is well posed for all initial data. While the full system of governing equations is obviously much more complex than these simple model equations, stability may still be improved by transforming the general three-dimensional system into an appropriate coordinate system where the problem is essentially two dimensional.

Osculating Plane

In a general, three-dimensional flowfield, the two dimensional plane within which the flow is locally two dimensional is called the osculating plane (OP). Both the velocity and acceleration vectors are contained in the OP; thus, there is no pressure gradient normal to the OP. By transforming the system of governing equations into a curvilinear coordinate system where one family of isosurfaces is everywhere tangent to the OP, the system becomes locally two dimensional in much the same way that an axisymmetric flowfield can be treated as globally two dimensional.

Governing Equations

The five equations governing the flowfields of this study are the conservation of mass, the conservation of momentum, and the conservation of entropy along streamlines, given in vector notation by

$$\mathbf{E}\boldsymbol{q}_x + \mathbf{F}\boldsymbol{q}_y + \mathbf{G}\boldsymbol{q}_z = 0 \tag{8}$$

where

$$\mathbf{E} = \begin{bmatrix} u & \rho & 0 & 0 & 0 \\ 0 & \rho u & 0 & 0 & 1 \\ 0 & 0 & \rho u & 0 & 1 \\ 0 & 0 & 0 & \rho u & 1 \\ -up\gamma & 0 & 0 & 0 & \rho u \end{bmatrix} \tag{9}$$

$$\mathbf{F} = \begin{bmatrix} v & 0 & \rho & 0 & 0 \\ 0 & \rho v & 0 & 0 & 1 \\ 0 & 0 & \rho v & 0 & 1 \\ 0 & 0 & 0 & \rho v & 1 \\ -vp\gamma & 0 & 0 & 0 & \rho v \end{bmatrix} \tag{10}$$

$$\mathbf{G} = \begin{bmatrix} w & 0 & 0 & \rho & 0 \\ 0 & \rho w & 0 & 0 & 1 \\ 0 & 0 & \rho w & 0 & 1 \\ 0 & 0 & 0 & \rho w & 1 \\ -wp\gamma & 0 & 0 & 0 & \rho w \end{bmatrix} \tag{11}$$

and

$$\boldsymbol{q} = [\rho \quad u \quad v \quad w \quad p]^T \tag{12}$$

The subscripts denote partial derivatives. The use of the entropy equation in place of the energy equation is valid for the inviscid, adiabatic flows considered here, and is used here because it lessens the coupling between the system of equations. The substitution of p/ρ^γ in place of the entropy is valid for calorically perfect gases.

Equations (8–12) are nondimensionalized using $\tilde{\rho} = \rho/\rho_\infty$, $\tilde{u} = u/a_\infty$, $\tilde{v} = v/a_\infty$, $\tilde{w} = w/a_\infty$, and $\tilde{p} = p/(p_\infty\gamma)$. When these relations are substituted into Eqs. (8–12), the system remains unchanged in form. For simplicity the tildes are dropped throughout the remainder of the development.

The equations are transformed into a generalized coordinate system where $\xi = \xi(x, y, z)$, $\eta = \eta(x, y, z)$, and $\zeta = \zeta(x, y, z)$. Expanding the partial derivatives using the chain rule, one obtains

$$\hat{\mathbf{E}}\boldsymbol{q}_\xi + \hat{\mathbf{F}}\boldsymbol{q}_\eta + \hat{\mathbf{G}}\boldsymbol{q}_\zeta = 0 \tag{13}$$

where

$$\hat{\mathbf{E}} = \begin{bmatrix} U & \rho\xi_x & \rho\xi_y & \rho\xi_z & 0 \\ 0 & \rho U & 0 & 0 & \xi_x \\ 0 & 0 & \rho U & 0 & \xi_y \\ 0 & 0 & 0 & \rho U & \xi_z \\ -Up\gamma & 0 & 0 & 0 & \rho U \end{bmatrix} \tag{14}$$

$$\hat{\mathbf{F}} = \begin{bmatrix} V & \rho\eta_x & \rho\eta_y & \rho\eta_z & 0 \\ 0 & \rho V & 0 & 0 & \eta_x \\ 0 & 0 & \rho V & 0 & \eta_y \\ 0 & 0 & 0 & \rho V & \eta_z \\ -Vp\gamma & 0 & 0 & 0 & \rho V \end{bmatrix} \tag{15}$$

and

$$\hat{\mathbf{G}} = \begin{bmatrix} W & \rho\zeta_x & \rho\zeta_y & \rho\zeta_z & 0 \\ 0 & \rho W & 0 & 0 & \zeta_x \\ 0 & 0 & \rho W & 0 & \zeta_y \\ 0 & 0 & 0 & \rho W & \zeta_z \\ -Wp\gamma & 0 & 0 & 0 & \rho W \end{bmatrix} \tag{16}$$

Here U, V, and W are the contravariant velocities in the ξ, η, and ζ directions, respectively, and ξ_x, ξ_y, ξ_z, η_x, η_y, η_z, ζ_x, ζ_y, and ζ_z are the inverse metrics.

As stated in the previous sections, marching within the OP reduces the effects of the ill-posedness. Within the OP the contravariant velocity V is by definition exactly zero. Setting $V = 0$ in Eq. (15), one obtains

$$\hat{\mathbf{E}}\boldsymbol{q}_\xi + \hat{\mathbf{F}}^*\boldsymbol{q}_\eta + \hat{\mathbf{G}}\boldsymbol{q}_\zeta = 0 \tag{17}$$

where

$$\hat{\mathbf{F}}^* = \begin{bmatrix} 0 & \rho\eta_x & \rho\eta_y & \rho\eta_z & 0 \\ 0 & 0 & 0 & 0 & \eta_x \\ 0 & 0 & 0 & 0 & \eta_y \\ 0 & 0 & 0 & 0 & \eta_z \\ 0 & 0 & 0 & 0 & 0 \end{bmatrix} \tag{18}$$

This is the system of equations that is used to describe the flowfield between the shock and the waverider lower surface.

Grid Generation

The computational grid is dependent on the solution; hence, it must be generated layer by layer as the solution is advanced. The marching directions are determined by setting $V = 0$ and by marching normal to the existing ξ-grid line. Marching distances are determined using a two dimensional method-of-characteristics philosophy. Details of the approach are given in Ref. 10.

Marching

On the shock surface and at each of the new grid planes determined by the marching procedure, the partial derivatives of the primitive variables with respect to ξ and η are computed using finite differences. Remaining are five equations and five unknowns: the five partial derivatives with respect to ζ. To solve for the ζ partial derivatives, the system is inverted, yielding

$$\boldsymbol{q}_\zeta = -\hat{\mathbf{G}}^{-1}\left(\hat{\mathbf{E}}\boldsymbol{q}_\xi + \hat{\mathbf{F}}^*\boldsymbol{q}_\eta\right) \tag{19}$$

Because of the sparseness of the matrix $\hat{\mathbf{G}}$, its inversion is easily performed. The ξ and η gradients are computed using second-order central differences, and the solution is advanced to a new grid plane by replacing the ζ partial derivatives in Eq. (19) with second-order central differences as well.

Boundary Conditions

The flowfields considered here are symmetric about $y = 0$, with the flow aligned in the positive x direction, and with the shock surface the $\zeta = 1$ boundary. The central-differenced marching step cannot be used at $\zeta = 1$, since no data are known at a previous step; consequently, first-order, one-sided differences are applied. Since marching is performed in the ζ direction, boundary conditions are not needed at an upper limit. The $\eta = 1$ boundary is the symmetry plane, and a symmetry condition is applied there. The upper limit of η is handled with second-order, one-sided differences. Data here are of minimal importance, as they generally lie outside the domain of interest for the waveriders. The boundaries at $\xi = 1$ and $\xi = \xi_{\max}$ are somewhat more complex. Based on a two dimensional method-of-characteristics philosophy, each new ζ grid plane is reduced by one point at each of these boundaries, so that second-order central differences can be used to impose explicit boundary conditions without introducing instabilities to the solution.

Waverider Design

The two surfaces of the waverider are designed independently, and the design of each utilizes a different approach. The methods used for each are outlined here.

Lower-Surface Design

As previously stated, the lower surface is defined by a streamsurface within a known flowfield. The method for defining the flowfield was described in the previous section. The streamsurface is approximated by many streamlines integrated downstream from a given leading edge. The leading edge is a curve in three-dimensional space that lies on the shock surface. Its shape defines both the flow capture tube and the planform of the resulting waverider.

Streamline integration is performed in the computational domain for simplicity. Recall that by marching in the OP, the contravariant velocity V is zero at every grid point; thus, the integration in computational space need only be two dimensional. Additionally, the computational grid is uniform with unit cells, further simplifying the computation. Integration is done using the fourth-order Runge–Kutta method. The streamline coordinates in the computational domain (ξ, η, ζ), are transformed into physical (Cartesian) space. All of the streamlines are combined to define the waverider lower surface (Fig. 3a), and the surface points are redistributed to form a more conventional mesh (Fig. 3b).

Upper-Surface Design

The upper-surface geometry is at the discretion of the designer. An option is available to generate expansion upper surfaces to enhance the overall vehicle performance. Expansion surfaces are created by first defining a freestream upper surface, and then applying a weighted average between the freestream surface and the lower surface. This averaging approach provides a flexible design method for generating open, partially closed, or closed trailing edges.

The flow parameters on the upper surface are predicted using an approximation to the axisymmetric method of characteristics. The first-order approach, developed and validated in Ref. 11, is robust, extremely fast, and sufficiently accurate.

Performance Evaluation

The lift and drag of the waveriders is computed by integrating the pressure forces over the surface of the waverider. The freestream

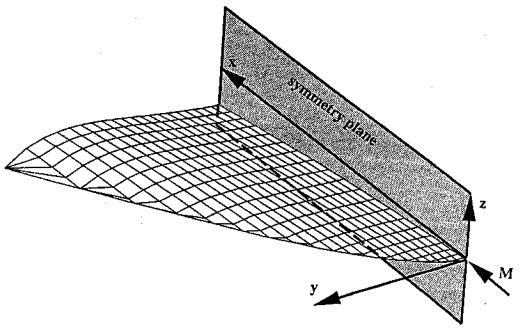

a) Streamline-oriented mesh

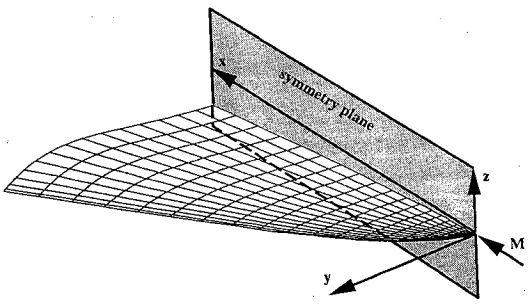

b) Redistributed mesh

Fig. 3 Lower-surface definition.

pressure is subtracted from the local pressure so that the pressure contributions on the upper and lower surfaces may be evaluated individually, and any contribution caused by a finite base area is removed. Nondimensional lift and drag coefficients are computed using the symmetry-plane chord length as a reference length and the integrated planform area as the reference area. Details of the integration algorithm are given in Ref. 10.

Results

Validation of the cross-stream marching algorithm, SCIEMAP (supersonic cross-stream inverse Euler marching program) can be found in Ref. 10, where comparisons with theory are used to validate the accuracy of the marching scheme for simple shock geometries such as planar or axisymmetric cone shocks, and results are compared with Rankine–Hugoniot or Taylor–Maccoll solutions, respectively. For most shock shapes of interest, however, closed-form solutions do not exist. By using the marching algorithm to design waverider vehicles, another means for validating the cross-stream marching code is made available. Direct simulations may be performed about the waveriders to see if the specified shock shape and resultant vehicle performance are duplicated.

Here the application to waverider design is evaluated, and comparisons are made to direct simulations of the resultant vehicles. Details of the methods used for the direct simulations can be found in Ref. 12. Computational grids about the waveriders are formed using the transfinite interpolation (TFI) grid generator HYGRID. The grids are modified during the solution procedure using a spline-fitting, solution-based grid adaption scheme, and solutions are produced using the F3D Euler solver.[13]

Five cases are presented with a range of more general shock geometries. All cases have a freestream Mach number of 4 with $\gamma = 1.4$. Computational grids for the direct simulations in all cases have $41 \times 63 \times 31$ points, and on the order of 2000 iterations are used to obtain converged solutions, with two intermediate grid refinement steps.

Sensitivity of the marching code to M_∞ and shock angle is discussed in Ref. 10. In short, the marching scheme does not have stability limits with reference to either, but grid generation becomes increasingly difficult as the shock strength becomes small. These five cases have sufficiently strong shocks such that grid generation is not a problem.

The first two cases have shocks cut from elliptic cones with elliptic axis ratios of $a/b = 0.75$ and 1.25, respectively, a symmetry-plane shock angle of 26.6 deg, and freestream upper surfaces. Case 3 has a shock cut from an axisymmetric cone with a 20.9-deg half angle at a 5.7-deg angle of attack, and the upper surface has a slight expansion. The shock in case 4 is cut from an axisymmetric surface with the shock angle varying from 27.7 deg at the nose to 25.6 deg at the exit plane to 20.3 deg at the downstream plane. A stronger expansion is used on the upper surface with a closed trailing edge on the outer portion of the body. The last case has a more general shock shape and is cut from a conoid with the same symmetry-plane profile as case 4 but with elliptic cross sections with $a/b = 0.65$. This waverider also has an expansion upper surface. Figures 4–8 illustrate the five waverider topologies, respectively. All five marching grids have 41 points in the streamwise and spanwise directions, and they have 12, 15, 16, 17, and 20 points in the marching direction, respectively. Note that, although the streamwise shock curvature in cases 4 and 5 is quite small, the effect on the flowfield is quite large, as can be seen in Fig. 9. Figure 9a portrays straight isolines, characteristic of conical flowfields, for case 2, but Fig. 9b portrays the much different flowfield of case 4, with the isolines curved by the variable shock strength.

Comparisons of nondimensional surface pressure on cross sections 90% downstream from the nose for the five cases are shown in Figs. 10–14. For cases 1 and 2 the agreement is excellent. The two codes differ somewhat near the leading edge, where the F3D Euler solver smears the shock over several grid cells and produces erroneous pressure oscillations across the shock. Agreement in the other three cases is quite good on the lower surface, with some discrepancy apparent on the upper-surface predictions, indicative of the first-order approach used there. The errors there are not large

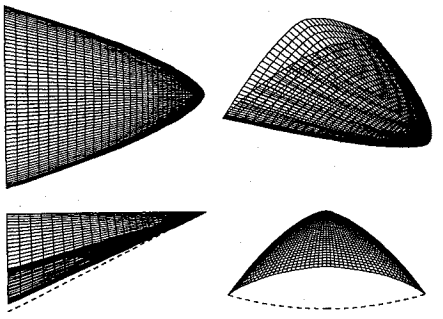

Fig. 4 Surface topology of case 1 (dashed curve: shock profile).

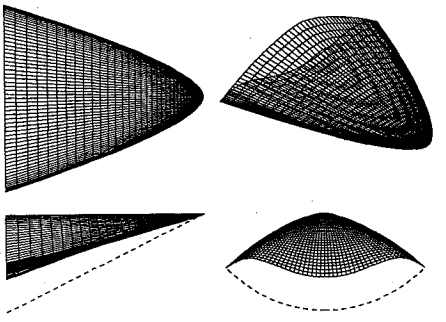

Fig. 5 Surface topology of case 2 (dashed curve: shock profile).

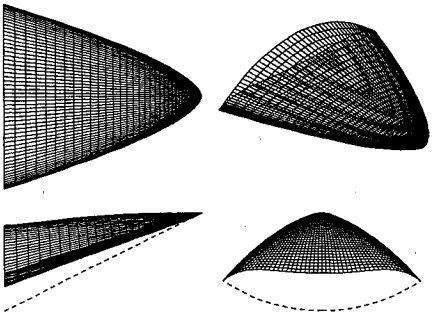

Fig. 6 Surface topology of case 3 (dashed curve: shock profile).

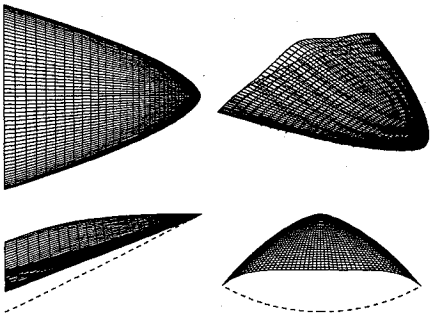

Fig. 7 Surface topology of case 4 (dashed curve: shock profile).

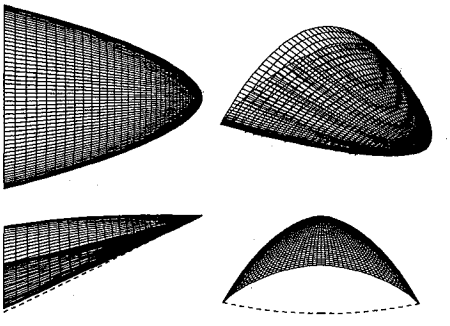

Fig. 8 Surface topology of case 5 (dashed curve: shock profile).

Table 1 Lift and drag results

Case	Code	C_l	C_d
1	SCIEMAP	0.2469	0.06609
	F3D	0.2444	0.06536
2	SCIEMAP	0.2403	0.06782
	F3D	0.2366	0.06669
3	SCIEMAP	0.2615	0.06948
	F3D	0.2605	0.06862
4	SCIEMAP	0.2630	0.06590
	F3D	0.2650	0.06590
5	SCIEMAP	0.2249	0.05246
	F3D	0.2263	0.05218

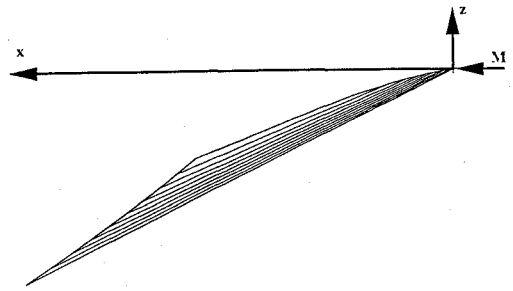

a) Case 2; conical flow (constant shock strength)

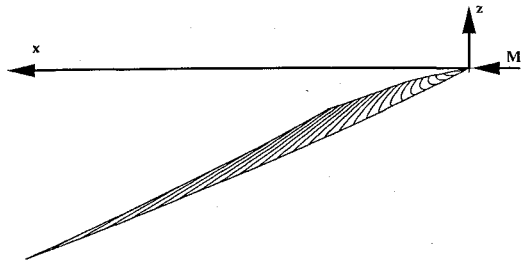

b) Case 4; nonconical flow (variable shock strength)

Fig. 9 Pressure isolines on the symmetry plane.

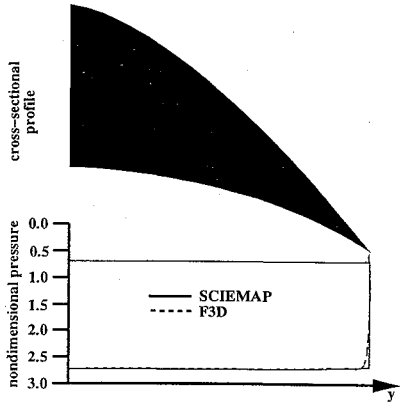

Fig. 10 Nondimensional surface pressure for case 1.

and are confined to quite small regions such that this error does not greatly influence the integrated results.

Integrated lift and drag coefficients for the five cases are presented in Table 1. Agreement is quite good in all cases. The expansion upper surfaces in cases 3, 4, and 5 account for 4.5%, 15%, and 6.2% of the total lift, respectively.

A further measure of the accuracy of the lower-surface design method may be estimated from entropy fluctuations along computed streamlines. Recall that for the isentropic postshock flows of this study, the entropy (or the entropy measure, p/ρ^{γ}) should be constant along streamlines. Each waverider lower surface is defined by 41 streamlines, and the variation of the entropy along each streamline, normalized by the streamline length, is computed. Maximum

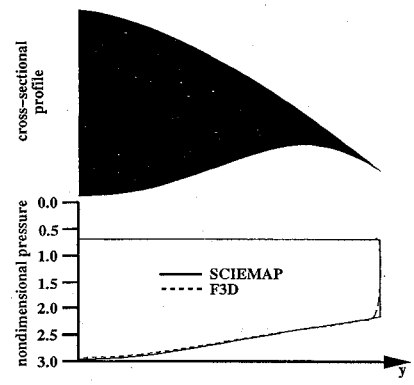

Fig. 11 Nondimensional surface pressure for case 2.

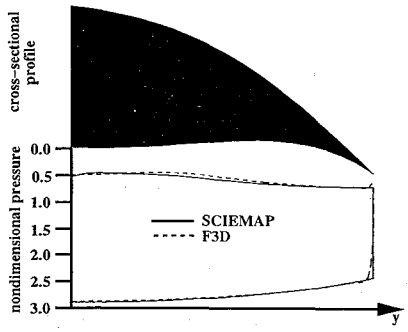

Fig. 12 Nondimensional surface pressure for case 3.

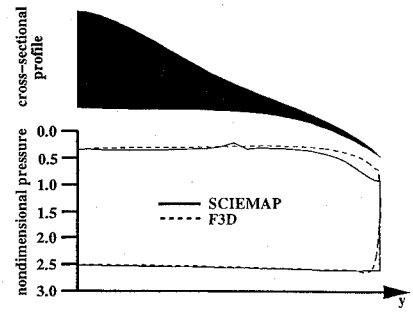

Fig. 13 Nondimensional surface pressure for case 4.

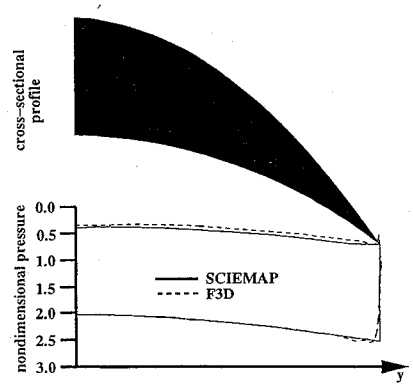

Fig. 14 Nondimensional surface pressure for case 5.

variations for the five cases are 0.02%, 0.05%, 0.04%, 0.17%, and 0.23%, respectively.

Conclusions

A new waverider design approach has been presented. The approach utilizes a cross-stream marching procedure that inversely generates a flowfield by marching the solution away from a prescribed shock surface. The new inverse solver provides a computationally efficient means for defining flowfields that were previously

unattainable. The application to waverider design affords a new class of general shock waveriders.

Five test cases were presented, demonstrating the versatility of the new approach for designing nonconical- and nonaxisymmetric-shock waveriders. Results were validated with direct simulations generated using the F3D Euler solver. Comparisons of pressure on the lower surface were excellent for all cases, and predictions were within expected tolerances on the expansion upper surfaces.

The new method requires only a few seconds to generate and evaluate an inviscid waverider, making it ideal for use in optimization studies. The addition of a boundary-layer code and other supplementary features would provide a leading-edge waverider design tool, providing greater flexibility than any past waverider design studies.

Acknowledgments

This work was supported by NASA Langley under Grant NAG-1-1295, by the Theoretical Fluids Branch of the DLR in Göttingen, Germany, and by the University of Colorado.

References

[1]Bauer, S. X. S., Covell, P. F., Forrest, D. K., and McGrath, B. E., "Preliminary Assessment of a Mach 4 and a Mach 6 Waverider," *Proceedings of the 1st International Hypersonic Waverider Symposium*, Oct. 1990.

[2]Kandebo, S. W., "Waverider Tests Boost Credibility," *Aviation Week and Space Technology*, Vol. 139, No. 11, 1993, pp. 61–63.

[3]Nonweiler, T. R. F., "Aerodynamic Problems of Manned Space Vehicles," *Journal of the Royal Aeronautical Society*, Vol. 63, Sept. 1959, pp. 521–528.

[4]Jones, J. G., "A Method for Designing Lifting Configurations for High Supersonic Speeds Using the Flow Fields of Non-Lifting Cones," Royal Aircraft Establishment, Rept. Aero. 2674, March 1963.

[5]Eggers, A. J., Jr., Ashley, H., Springer, G. S., Bowles, J. V., and Ardema, M. D., "Hypersonic Waverider Configurations From the 1950's to the 1990's," *Proceedings of the 1st International Hypersonic Waverider Symposium*, Oct. 1990.

[6]Center, K. B., Jones, K. D., Dougherty, F. C., Seebass, A. R., and Sobieczky, H., "Interactive Hypersonic Waverider Design and Optimization," *Proceedings of the 18th Congress of ICAS* (Beijing, PRC), Sept. 1992, pp. 1571–1580 (Paper ICAS-92-1.8.3).

[7]Bowcutt, K. G., "Optimization of Hypersonic Waveriders Derived from Cone Flows—Including Viscous Effects," Ph.D. Dissertation, Dept. of Aerospace Engineering, Univ. of Maryland, 1986.

[8]Jones, K. D., Bauer, S. X. S., and Dougherty, F. C., "Hypersonic Waverider Analysis: A Comparison of Numerical and Experimental Results," AIAA Paper 91-1696, June 1991.

[9]Sobieczky, H., Dougherty, F. C., and Jones, K. D., "Hypersonic Waverider Design from Given Shock Waves," *Proceedings of the 1st International Hypersonic Waverider Symposium*, Oct. 1990.

[10]Jones, K. D., "A New Inverse Method for Generating High-Speed Aerodynamic Flows With Application to Waverider Design," Ph.D. Dissertation, Dept. of Aerospace Engineering Sciences, Univ. of Colorado, Boulder, CO, May 1993.

[11]Center, K. B., "An Interactive Approach to the Design and Optimization of Practical Hypersonic Waveriders," Ph.D. Dissertation, Dept. of Aerospace Engineering Sciences, Univ. of Colorado, Aug. 1993.

[12]Jones, K. D., and Dougherty, F. C., "Numerical Simulation of High-Speed Flows About Waveriders with Sharp Leading Edges," *Journal of Spacecraft and Rockets*, Vol. 29, No. 5, 1992, pp. 661–667.

[13]Ying, S. X., Steger, J. L., Schiff, L. B., and Baganoff, D., "Numerical Simulation of Unsteady, Viscous, High-Angle-of-Attack Flows Using a Partially Flux-Split Algorithm," AIAA Paper 86-2179, Aug. 1986.

J. C. Adams
Associate Editor